Journal of Inorganic and Organometallic Polymers and Materials
https://doi.org/10.1007/s10904-023-02820-8

RESEARCH

Facile Synthesis of Ni^{2+} Doped $MgFe_2O_4$ Spinel Nanoparticles: Structural, Optical, Magnetic, and Dielectric Behavior

R. Revathi[1] · M. Sukumar[2] · Anuj Kumar[3] · Manish Gupta[4] · P. Aji Udhaya[5] · Satbir S. Sehgal[6] · Bidhan Pandit[7] · M. Sundararajan[8] · A. Subramani[9] · Chandra Sekhar Dash[10] · N. Senthilkumar[11] · Mohd Ubaidullah[12]

Received: 4 May 2023 / Accepted: 3 August 2023

Abstract

Nickel-doped magnesium cubic spinel ferrite nanoparticles (NPs) were prepared through the microwave combustion method (MCM). The structure of magnesium ferrite normal spinel is obtained from XRD analysis. The average crystallite size is between 26 and 17 nm. The elemental compositions and oxidizing states of Ni^{2+} doped $MgFe_2O_4$ ferrites were evaluated by using XPS analysis. The morphology of spinel nanoparticles was studied using HR-SEM images. The energy dispersive X-ray method is used for ensuring the presence of elements and the band gap value 2.09, 2.02, 1.85, and 1.82 eV have been obtained using the tau'c relation. The magnesium spinel structure is confirmed in the band at 434 and 561 cm^{-1} which corresponds to the stretching vibration of the octahedral site (Mg^{2+}–O^{2-}) and tetrahedral site (Fe^{3+}–O^{2-}) respectively. From the hysteresis loops the magnetic features viz. H_c, M_r, and M_s were determined. Further dielectric studies and AC conductivity of the prepared samples are performed.

Keywords Magnesium ferrite · Surface chemistry · Band gap · Ferromagnetism · Dielectric properties

✉ M. Sukumar
msukumsc@gmail.com

✉ M. Sundararajan
sundar15msc@gmail.com

✉ Chandra Sekhar Dash
chandu0071@gmail.com

✉ Mohd Ubaidullah
mtayyab@ksu.edu.sa

[1] Department of Biotechnology, Periyar University Centre for Post Graduate and Research Studies, Dharmapuri, Tamil Nadu 635 205, India

[2] Department of Applied Physics, Sri Venkateswara College of Engineering, Pennalur, Sriperumbudur, Tamil Nadu 602 117, India

[3] Department of Chemistry, GLA University, Mathura 281406, India

[4] Division of Research and Development, Lovely Professional University, Punjab, India

[5] Department of Physics, Holy Cross College (Autonomous), Nagercoil, Tamilnadu 629 004, India

[6] Division of Research Innovation, Uttaranchal University, Dehradun, India

[7] Department of Materials Science and Engineering and Chemical Engineering, Universidad Carlos III de Madrid, Avenida de la Universidad 30, Leganés, 28911 Madrid, Spain

[8] PG & Research Department of Physics, Paavendhar College of Arts & Science, M.V. South, Thalaivasal, Salem, Tamilnadu 636 121, India

[9] Department of Biochemistry, Dwaraka Doss Goverdhan Doss Vaishnav College, Chennai, Tamilnadu 600 106, India

[10] Department of Electronics and Communication Engineering, Centurion University of Technology and Management, Bhubaneswar, Odisha 752050, India

[11] Department of Chemistry, Graphic Era (Deemed to be University), Bell Road, Clement Town, Dehradun, Uttarakhand 248002, India

[12] Department of Chemistry, College of Science, King Saud University, P.O. Box 2455, 11451 Riyadh, Saudi Arabia

Published online: 26 August 2023

1 Introduction

Due to their unique structural, optical, electrical, and magnetic properties, nanomaterials have recently attracted a great deal of attention in the domains of nanoscience and nanotechnology [1, 2]. In the spinel family, magnetic ferrite nanomaterials are the most common because of their novel properties and wide range of applications [3–6]. Some examples include magnetic tapes for video and audio cartridges, data and energy/memory storage, magnetic ferrofluids, nano-magnetic medicine, resistive random access memory (RRAM), and magnetic hyperthermia.

Generally, the cubic spinel structure AB_2O_4, where A and B represent the tetrahedral A site for the Mg^{2+} ion (divalent metal) and the octahedral B site for the Fe^{3+} ion (trivalent metal). A crucial member of the spinel family is magnesium ferrite ($MgFe_2O_4$), which is a soft magnetic behavior and also n-type semiconducting material. Magnetic nanoparticles with a spinel structure are known as spinel ferrites. Due to their crystal structures and physical properties, magnetic nanoparticles are a type of spinel with the general formula MFe_2O_4 (M = Fe, Zn, Ni, Co, etc.) [7, 8].

The interaction between ionic species in the tetrahedral site (Mg-ions which is an A-site) and octahedral (Fe-ions which is B-site), including A-B exchange, B-B exchange, and A-A exchange, is what gives spinel nano-ferrites their magnetism. As a result, the cation species distribution in the A-site and B-site is related to the magnetic properties of spinel. Spinel ferrites' characteristics are influenced by the production process, chemical makeup, and cation dispersion [9]. In addition to uses for its magnetization, it can be utilized in sensor technologies, adsorption and humidity sensors, oxygen sensors, and heterogeneous catalysts.

Doping by transition or rare-earth elements led to the destruction of the spin cycloid due to a reduction in oxygen vacancies, as well as an increase in remanent polarisation, spontaneous magnetization, high switchable current, large absorption coefficient, magnetoelectric effect, and physical properties such as structural, optical, electrical, chemical and other properties of materials and therefore analysis of doping effects is of great interest in the fields of fundamental and applied science [10–12].

Nickel-doped magnesium ferrite is a soft ferrite category, widely used in device applications such as radio frequency, rod antenna, read/write memory, filters, transformer cores, delivery devices, biomedical, data storage, ferrofluids, and microwave absorption [13, 14]. There are several techniques to perform the synthesis of magnesium ferrite such as hydrothermal, ball milling, sol–gel, co-precipitation, electrospinning method, and combustion [15–20]. Furthermore, it was found that the approaches were too challenging to synthesize, expensive, time-consuming, etc.

In addition to the preceding techniques, nickel-doped magnesium ferrite spinel nanoparticles can also be created using MCM. Microwave energy, by its very nature, produces a rapid rise in the temperature of the precursor due to the significant intermolecular friction involved. MCM approach and other physical characterization investigations are utilized to completely investigate the structural, morphological, optical, magnetic, and dielectric properties for upcoming findings sections.

2 Experimental Procedure

2.1 Materials and Preparation Process

Ferric nitrate, magnesium nitrate, nickel nitrate, and L-arginine were purchased from Merck, India, and they were utilized as obtained deprived of any further purification, for sample preparation. $Ni_{1-x}Mg_xFe_2O_4$ ($0 \le x \le 0.5$) NPs were synthesized by varying the fraction x between 0.0 to 0.5 mol percentage. The precursors are comprised of magnesium nitrate, ferric nitrate, and nickel nitrate, where all nitrates

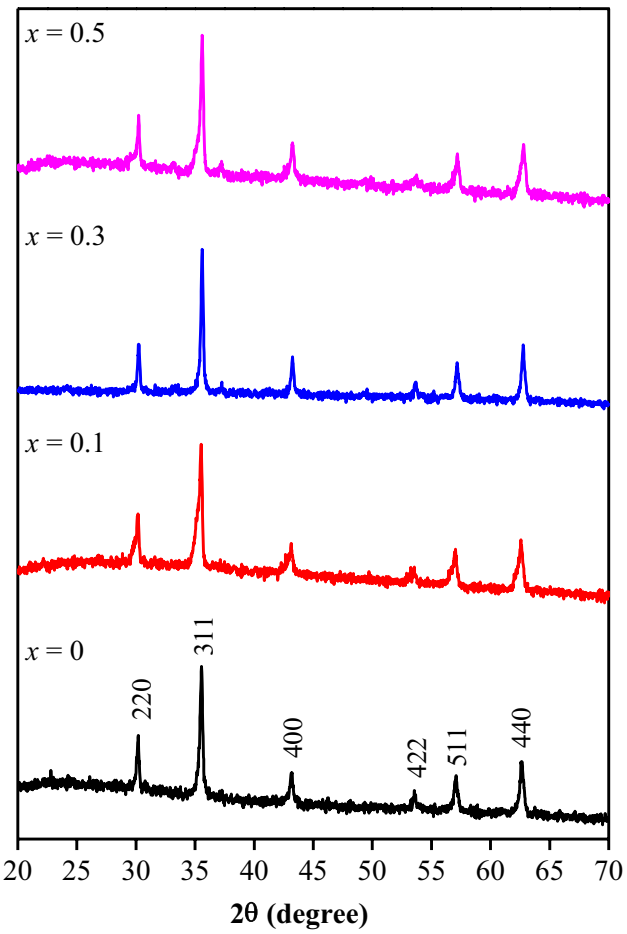

Fig. 1 XRD spectra of Ni-doped $MgFe_2O_4$ spinel nanoparticles

Table 1 XRD parameters and optical band gap of MNFO system

Ni^{2+} fraction, x	Average crystallite size, D (nm) by Scherrer's formula	Effective particle size, L (nm) by Williamson–Hall plot	Lattice parameter, a (Å)	Cell volume ($Å^3$)	Band gap, Eg (eV)
$x=0$	26	25	8.319	575.72	2.09
$x=0.1$	24	22	8.323	576.55	2.02
$x=0.3$	19	17	8.331	578.21	1.85
$x=0.5$	17	16	8.400	592.70	1.82

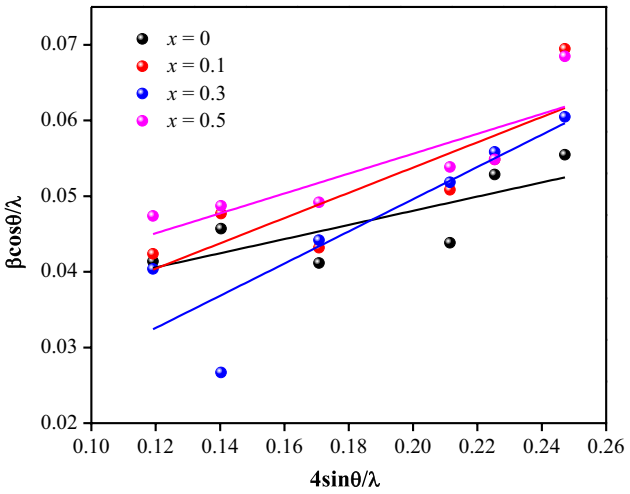

Fig. 2 W–H plot of Ni-doped $MgFe_2O_4$ nanoparticles

serve as oxidizers and L-arginine is employed as fuel. The precursors for $Ni_{1-x}Mg_xFe_2O_4$ and L-arginine are poured into a beaker comprising de-ionized and rigorous stirring at room temperature was performed until (≈ 45 min) a homogenous solution is obtained. The fuel-to-oxidizer ratio (F/O) was assumed to be 1 by propellant chemistry principles [21–23]. The required amount of oxidizer-to-fuel molar ratio for the composition was calculated based on the total oxidizing and reducing valences in the oxidizer (nickel nitrate, magnesium nitrate, ferric nitrate) and dividing by the sum of the total oxidizing and reducing valences in the fuel as expressed in the following equation [24].

$$\frac{Oxidizer}{Fuel} = \frac{\sum all\ oxidizing\ and\ reducing\ elements\ in\ oxidizer}{(-1)\sum oxidizing\ and\ reducing\ elements\ in\ fuel} \quad (1)$$

The homogenous solution is then transferred to a silica crucible and heated in a 900 W (≈ 150 – 170 °C) microwave oven (Samsung, India Limited) for 10 min at an irradiation frequency of 2.54 GHz. Once the temperature reached a threshold level, the precursor solution underwent dehydration and combustion, resulting is a black fluffy powder. Upon boiling, the temperature reached a threshold level, the precursor solution underwent dehydration and combustion, which caused gas evolution. Once spontaneous combustion is attained ignition happens with a rapid flame causing the creation of solid fluffy final products of $Mg_{1-x}Ni_xFe_2O_4$ ($x=0$ to 0.5) nanoparticles were obtained. This black powder contained metal hydroxides and other impurity phases, and it was subsequently subjected to annealing at 500 °C for 2 h, resulting in the formation of the crystalline Ni-doped $MgFe_2O_4$ phases of the spinel system. The compositions were prepared with the addition of cobalt (Ni^{2+}) of different molar ratios in an $Mg_{1-x}Ni_xFe_2O_4$ system with $x=0$, 0.1, 0.3, and 0.5 and the samples are labeled as same.

2.2 Characterization Techniques

Rigaku Ultima IV high-resolution X-ray powder diffractometer of MNFO system examined crystal structure and phase composition. In this 2θ values were ranged from 20° to 80° using CuKα radiation at λ = 1.5418 Å. A KRATOS-AXIS Ultra DLD apparatus measured XPS using Al Kα radiation (E = 1486.6 eV) at 10 milliamps and 13,000 eV with high resolution 20 eV. The morphology and elemental information are acquired using an FEI Quanta FEG 200 SEM/EDX analyser The Thermo Scientific UV-DRS spectra were collected from 200 to 800 nm. The FT-IR spectrum was examined using Perkin Elmer (RX1) FT-IR spectrophotometer. VSM analysis performed well at RT using Lake Shore, USA, Model 7404 with 3 magnets.

3 Results and Discussion

3.1 XRD Analysis

The crystalline structure of nickel-doped magnesium ferrite nanoparticles is attained by XRD studies and the obtained diffractogram is depicted in Fig. 1, and it further confirmed the prepared samples are crystalline in nature. The angular position at 2θ values of 30.11°, 35.48°, 43.21°, 53.95°, 57.30° and 62.93° matched with reflections planes (220), (311), (400), (422), (511) and (440) respectively. The witnessed diffractogram was found to be in line with $MgFe_2O_4$ Nanoparticles (JCPDS card no. 89-3084). The synthesized nanoparticles belong to the magnesium spinel structure and

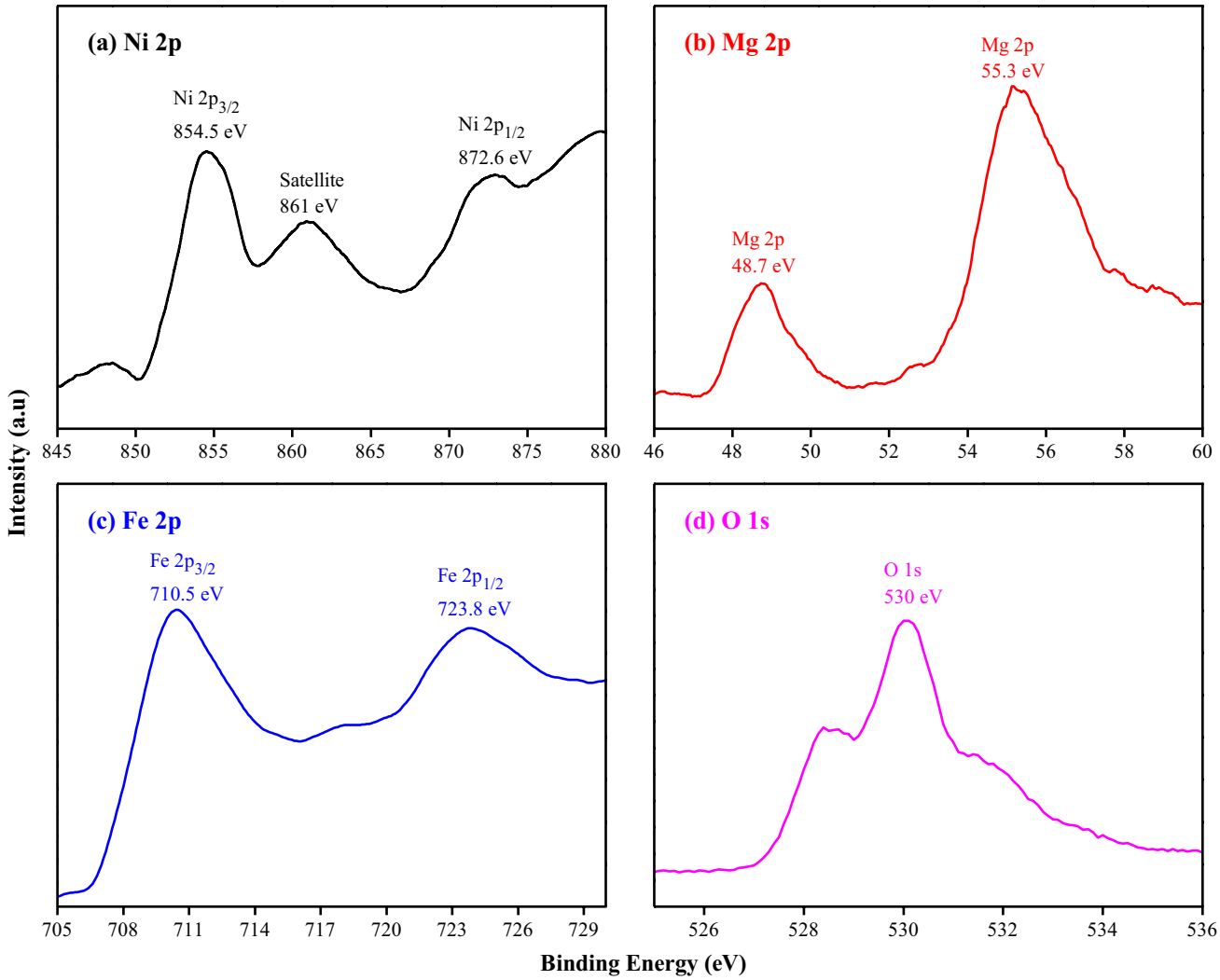

Fig. 3 XPS spectra of **a** Ni 2p; **b** Mg 2p; **c** Fe 2p; **d** O 1s elements for Ni ($x = 0.5$)-doped $MgFe_2O_4$ spinel nanoparticles

$Fd\bar{3}m$ space group. The impurity peaks were observed in nickel-doped magnesium ferrite [25–27].

The Eq. (1) found the lattice parameters as follows,

$$a = d_{hkl}\sqrt{(h^2 + k^2 + l^2)} \tag{1}$$

where, h, k, and l are the Miller indices, *a,* is the lattice parameter and d_{hkl}, is the interplanar spacing corresponding to the Miller indices. The deduced lattice parameters are summarized in Table 1. The lattice parameter *'a'* attained for the pure $MgFe_2O_4$ is found to be in line with values testified in earlier studies (8.371 Å) by Baskar et al. [26] and Hema et al. [28]. As the lattice parameters were found to decrease with a rise in the concentration of Mg^{2+} which infers that it relates linearly to Vegard's Law. The lattice parameter rises linearly with an increase in Ni^{2+} concentration which points to the existence of the symmetry and contraction of the lattice. As Mg^{2+} (ion radius 0.72 Å) ions replace Ni^{2+} (ion radius 0.69 Å) ions in the regular spinel structure, resulting in crystal lattice contraction [29].

Using Debye Scherrer's Eq. (2) average crystallite size (L) is deduced.

$$L = \frac{0.89\lambda}{\beta \cos\theta} \tag{2}$$

where, L, is the size of the crystallite; λ, the wavelength; β, represents the full width at half maximum; and 2θ, the diffraction angle. The size of the crystallite for Ni^{2+} doped $MgFe_2O_4$ (x = 0, 0.1, 0.3, and 0.5) spinel nanoparticles

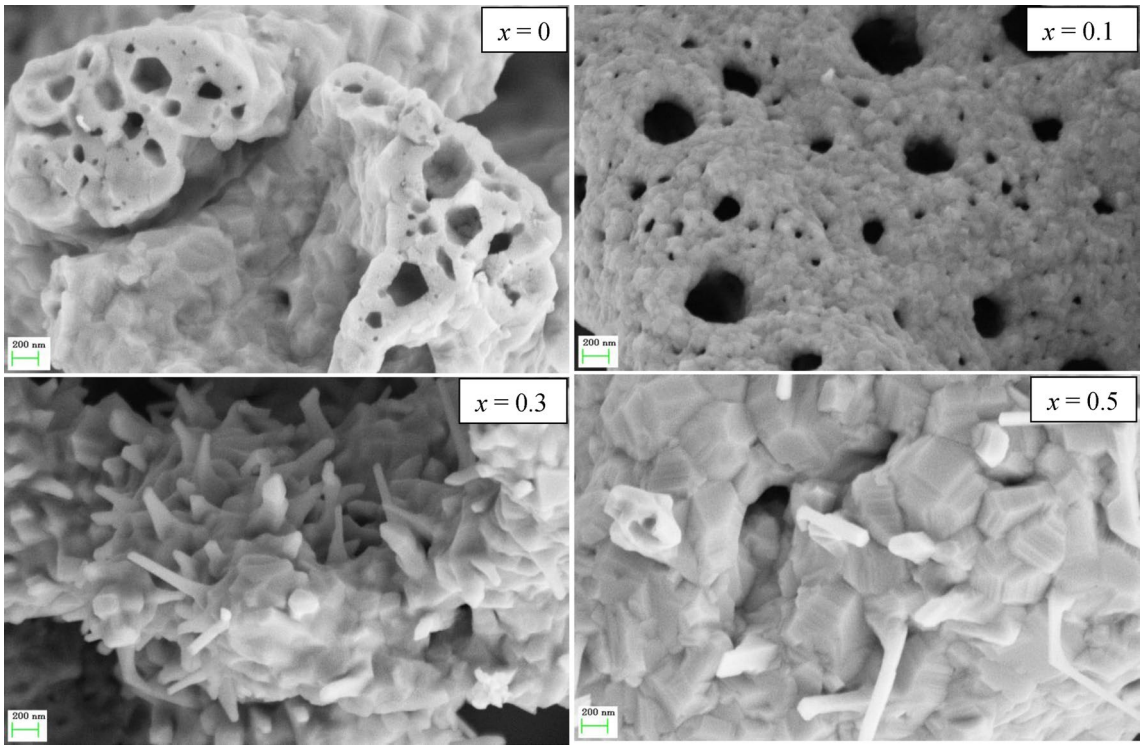

Fig. 4 HR-SEM analysis of MNFO system

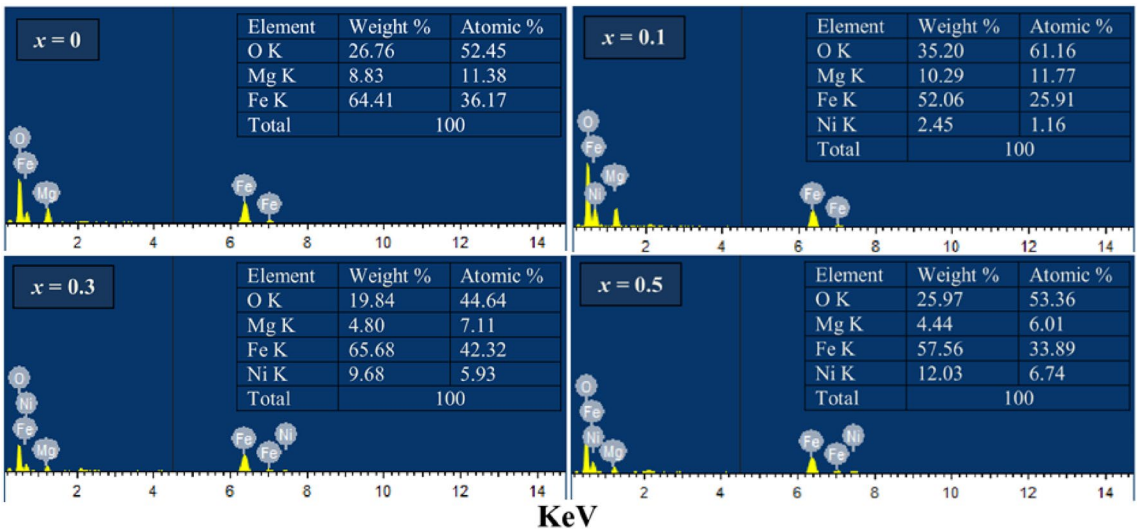

Fig. 5 EDX spectra of Ni-doped $MgFe_2O_4$ spinel nanoparticles

gradually decreased; it was reported in the literature. This can be explained by differences between the ionic radii of the Mg^{2+} and Ni^{2+} ions in the parent MgFe2O4 spinel system. Due to the smaller size of Ni2 + ions, the diffusion rate is enhanced in the Ni-doped MgFe2O4 spinel nanoparticles. Another reason may be due to controlled by the nucleation and particle growth [30].

The effective particle sizes (L) and the strain (ε) component were also evaluated using the Williamson–Hall (W–H) method given in Eq. (3):

$$\frac{\beta \cos\theta}{\lambda} = \frac{k}{L} + \frac{4\varepsilon \sin\theta}{\lambda} \tag{3}$$

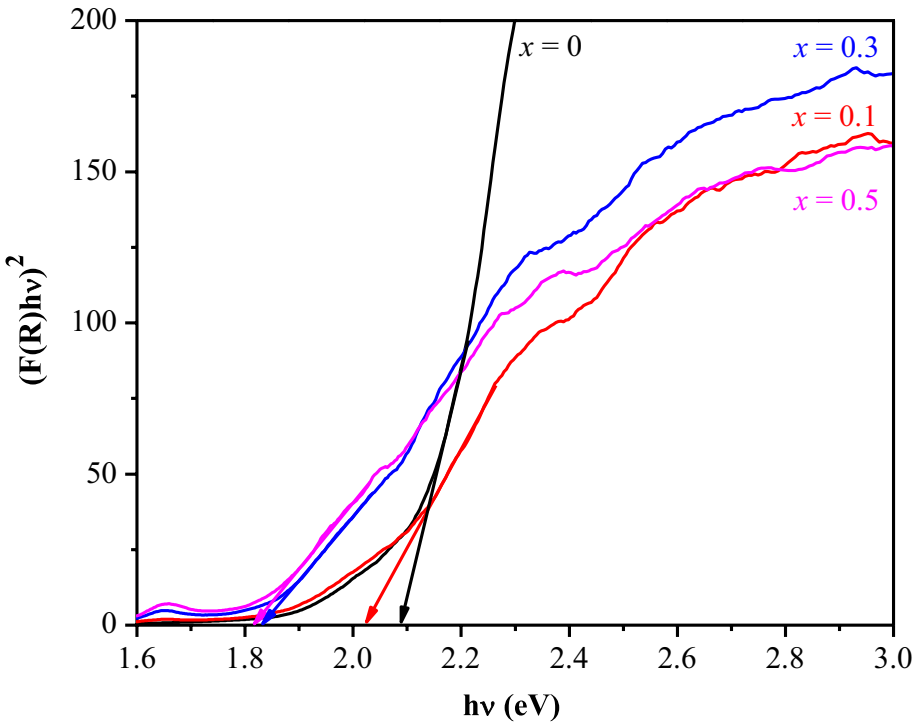

Fig. 6 $(F(R)h\upsilon)^2$ vs $E\ (h\upsilon)$ of MNFO system

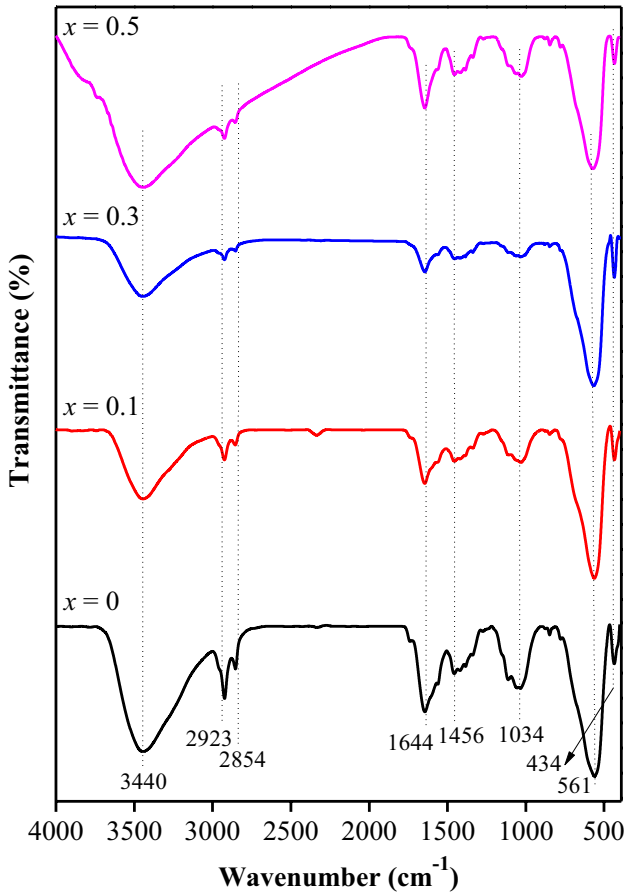

Fig. 7 FT-IR spectra of Ni-doped $MgFe_2O_4$ spinel nanoparticles

where, k is a constant (0.89), and ε is the strain associated with the nanoparticles. Equation (4) represents a straight line between 4sinθ/λ and βcosθ/λ. The slope of this line gives the strain (ε), while the intercept (k/L) on the y-axis gives the effective crystallite size (L). Figure 2 shows the W–H plots of Ni-doped $MgFe_2O_4$ spinel system. A variation in the effective crystal size was noticed using the Debye–Scherrer's formula (see Table 1). The difference may be due to effect of internal strain not considered in the Scherrer model. The appearance of a positive slope in Fig. 2 indicates the possibility of tensile strain in the samples.

3.2 XPS Analysis

Figure 3 shows that, to determine the surface composition and oxidation states were used XPS spectra of the MNFO system. Figure 3a shows the Ni 2p peaks located at 854.5 eV and 872.6 eV representing the Ni $2p_{3/2}$ and Ni $2p_{1/2}$, respectively, which indicates the presence of Ni^{2+} oxidation state with satellite peaks at 861 eV consistently [3]. In Mg 2p region, as shown in Fig. 3b, two strong peaks at the binding energies of 48.7 eV and 55.3 eV respectively. The first peak shows lower binding energy corresponding to a very small fraction of A-site Mg^{2+} ions and the second intense peak shows a large amount of B-site Mg^{2+} ions [31]. Figure 3c displayed a high-resolution spectrum of Fe 2p and two distinct peaks were observed at around 710.5 eV and 723.8 eV, corresponding to the Fe $2p_{3/2}$ and Fe $2p_{1/2}$, respectively.

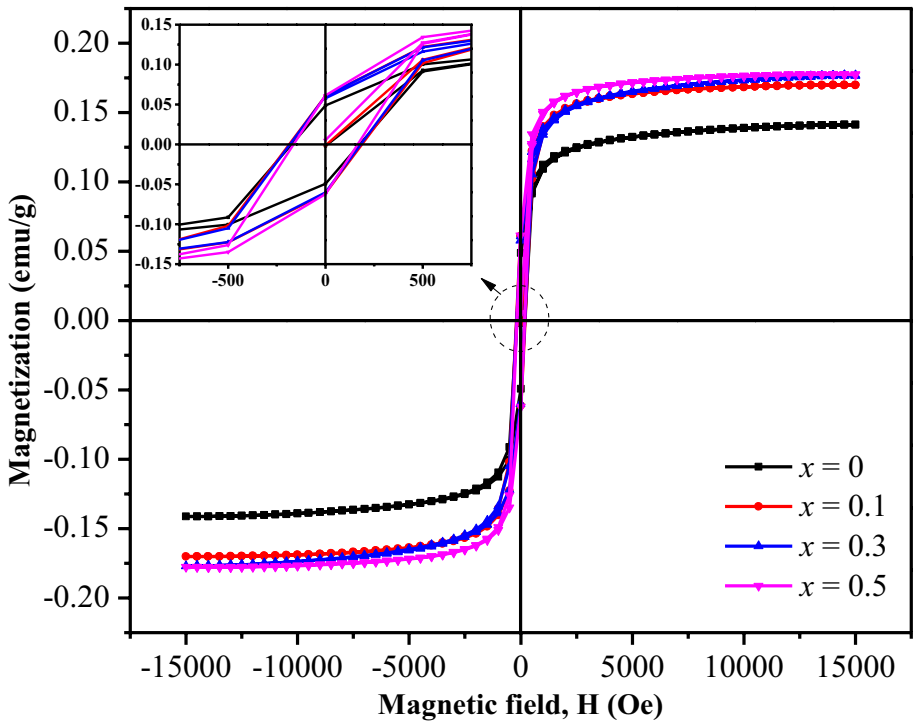

Fig. 8 Magnetic hysteresis curves of MNFO system

Table 2 Magnetic parameters of Ni doped $MgFe_2O_4$ spinel nanoparticles

Ni^{2+} fraction, x	Coercivity, H_c (Oe)	Remanence, M_r(memu/g)	Saturation Magnetization, M_s(emu/g)
$x=0$	174.51	48.972	0.141
$x=0.1$	187.28	61.062	0.170
$x=0.3$	182.39	60.371	0.176
$x=0.5$	164.47	61.794	0.178

Figure 3d shows the O 1 s XPS spectra in the Ni^{2+} doped $MgFe_2O_4$ nanoparticles. The peak at 530 eV is attributed to the hydroxyl oxygen and the lattice oxygen, respectively [3].

3.3 HR-SEM and EDX Analysis

As seen in Fig. 4, Ni doped $MgFe_2O_4$ spinel nanoparticles had uneven shapes and severe agglomeration. The agglomeration of nanoparticles is associated with the microwave combustion process in the presence of L- arginine. The microstructure changes from small-sized isolated grains surrounding pores into intra-granular pores with partly distinct particles that are fused with other grains for (x = 0 and 0.1), then flower-like particles for (x = 0.3). Further, an increase in higher doping concentration (x = 0.5) of rectangular-shaped particles was obtained. In addition, Fig. 5 showed the EDX analyses of $Mg_{1-x}Ni_xFe_2O_4$ spinel nanoparticles. The peak of Mg, Ni, Fe, and O elements and the inset table illustrates their elemental composition fractions (see Fig. 5).

3.4 DRS-UV Analysis

DRS were recorded for the Ni-doped $MgFe_2O_4$ system. Using the Kubelka–Munk function the values of the optical band gap is determined using Eq. (4)

$$F(R)h\nu = A\left(h\nu - E_g\right)^n \tag{4}$$

The plots between $(F(R)h\nu)^2$ versus $h\nu$ and spreading out the x-axis for all the samples are shown in Fig. 6. When the linear regions are subjected to extrapolation $(F(R)h\nu)^2 = 0$) provide values of the direct band gap. The values of the energy gap were found to lie in the range of 2.09, 2.02, 1.85, and 1.82 eV. The band gap value of pure $MgFe_2O_4$ spinel nanoparticles prepared in this study is found to be lower than the values (2.62 eV) and (2.14 eV) reported in the literature [26, 30], this may be due to quantum confinement effect. The values of the band gap rise within a surge in Ni^{2+} concentration in $MgFe_2O_4$ spinel system. The existence of a weak quantum size effect in the nano-regime is ensured by the decline in optical band gap values, which occurred as Mg^{2+} ions occupied the octahedral positions resulting in the creation of shallow traps. The fall in optical band gap value indicates weak quantum size impact at the nano-regime and may explain

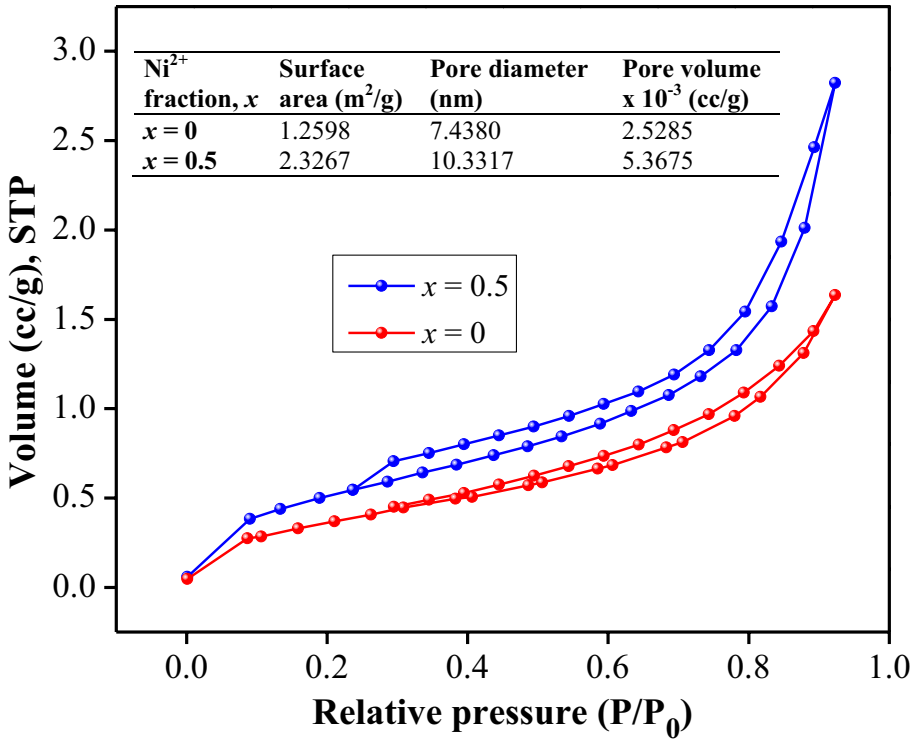

Fig. 9 BET measurements of Ni-MNFO spinel nanoparticles

why most Mg^{2+} occupied octahedral sites and formed shallow traps [32].

3.5 FT-IR Studies

Figure 7 shows MNFO system FT-IR spectra from 4000 to 400 cm^{-1} wavenumber. The water mole atop magnesium ferrite samples causes the 3440 cm^{-1} peak. C-H stretching vibration caused 2923 and 2854 cm^{-1} peaks. H–O-H water bending vibration causes the 1644 cm^{-1} band. O–H stretching vibrations from adsorbed H_2O cause the 1456 cm^{-1} band [33–35]. The absorption bands at 1034, 561, and 434 cm^{-1} correspond to stretching vibrations of tetrahedral sites (Metal–Oxygen bonds) and octahedral sites, respectively [36–40].

3.6 Magnetization Analysis

The magnetization behavior of $Mg_{1-x}Ni_xFe_2O_4$ Nanoparticles was studied at room temperature and the applied field was in the range of -15 kOe to + 15 kOe as shown in Fig. 8, which indicates it is of the soft ferrite category. With the aid of M-H plots, the parameters viz. M_r, H_c, and M_s were estimated. For $x = 0$, the value of the coercivity was found to be 174.51 Oe which further decreased to 187.28 Oe for $x = 0.1$. Furthermore, its value has risen to 182.39 Oe for $x = 0.2$ which then declines $x = 0.3$ to 0.5 (164.47 Oe) with the rise in Ni^{2+} ion concentration as shown in Table 2. The factors viz. surface defects and cation redistribution account for the alteration of total magnetic moments which cause a decline in coercivity value [13, 41–43]. An increase in the values of M_r and M_s from 48.972, 61.062, 60.371, 61.794, emu/g and 0.141, 0.170, 0.176, 0.178 for $x = 0$ to 0.5 respectively. The saturation magnetization values increase with the increasing of the Ni concentration in the $MgFe_2O_4$, it may due to cation distribution variance on tetrahedral and octahedral sites, and particles size effect, surface spin effect, and chemical composition respectively. The growth in surface spin disorder corresponds to the improved surface anisotropy. As the spinel nanoparticles with the best surface anisotropy differs from one shape to another shape. The saturation magnetization values significantly increase suggesting a reduced disarranging effect of surface spins in the samples with enhanced particle size, which is further confirmed by the SEM images [43].

3.7 N_2 Adsorption–Desorption Isotherms

The surface area has been determined from the N_2 adsorption–desorption isotherms recorded at 77 K using the BET technique as shown in Fig. 9. The undoped ($x = 0$) and Ni-doped $MgFe_2O_4$ ($x = 0.5$) spinel nanoparticles exhibited mixture isotherms of type II and type IV, respectively. Hysteresis loops exist in the large P/P_0 range, which indicates the creation of mesopores in the Ni-doped $MgFe_2O_4$ spinel nanoparticles. The inset in Fig. 9 shows the surface and pore characteristics. The values of surface area, pore diameter

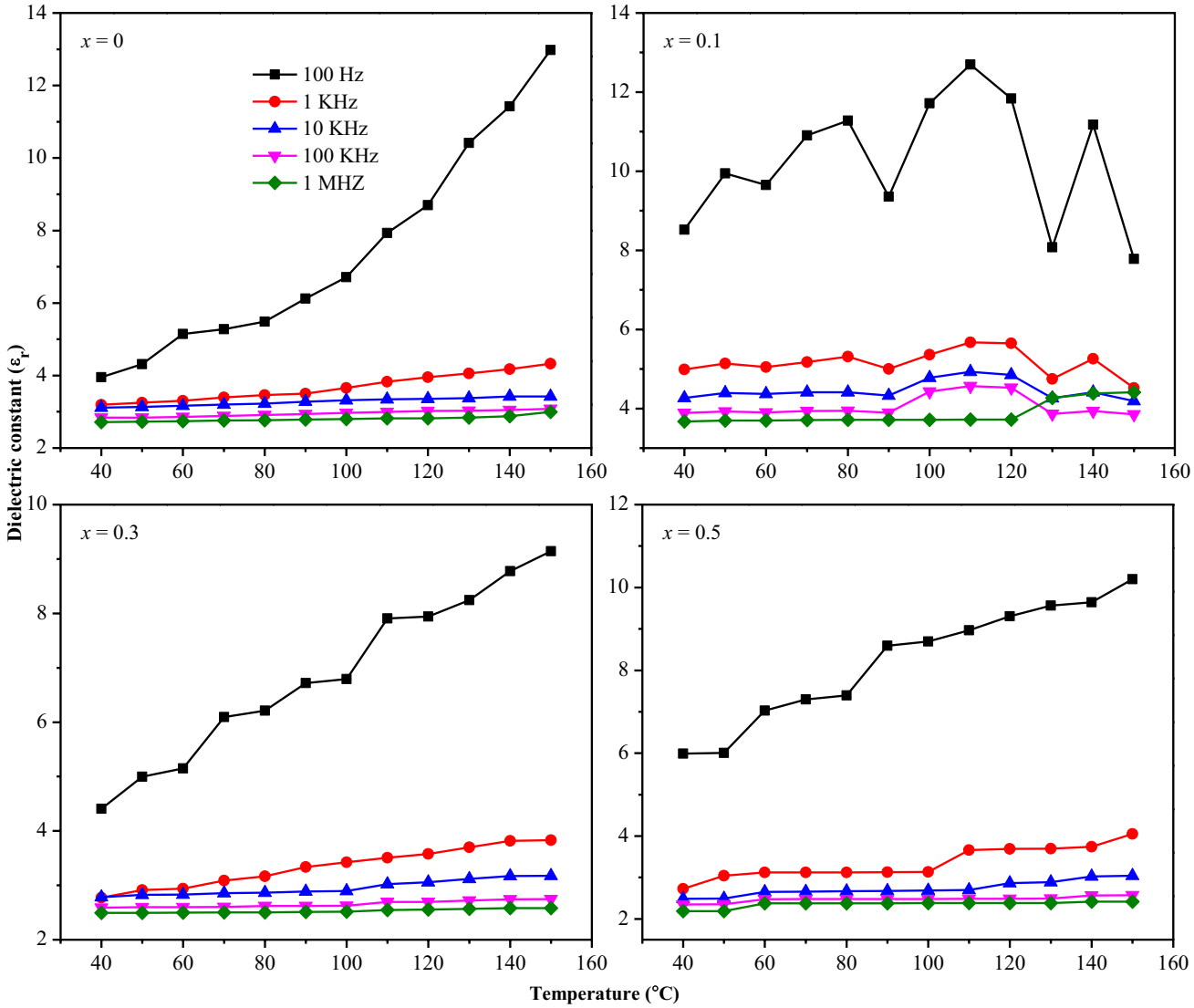

Fig. 10 Dielectric constant of Ni-doped $MgFe_2O_4$ spinel nanoparticles

and pore volume are increased gradually with increased Ni concentration [10, 18].

3.8 Dielectric Properties

Spinel ferrites are an important class of compounds with diverse electrical, magnetic, and catalytic properties due to their high resistivity and low eddy current losses. The procedures utilized to prepare these ferrites have a substantial impact on their dielectric properties. It is also helpful to be aware of the material's dielectric properties. The prepared ferrite Ni-doped $MgFe_2O_4$ ($x=0$, 0.1, 0.3, and 0.5) spinel nanoparticles were subjected to dielectric study by using AGILENT 4284 A precision LCR meter to measure their dielectric constant and ac conductivity throughout different temperatures (from 313 to 423 K) and frequency range (from 100 Hz to 1 MHz), respectively. Using a 3-ton hydraulic press, we pelletized the Ni: $MgFe_2O_4$ ($x=0$, 0.1, 0.3, and 0.5) samples such that one side would serve as an electrode and the other as a parallel plate capacitor covered with high-purity silver paste. The dielectric constant of Ni-doped $MgFe_2O_4$ ($x=0$, 0.1, 0.3, and 0.5) samples concerning temperature at varying frequencies is shown in Fig. 8. Using the formula,

$$\varepsilon_r = CD/\varepsilon_0 A \tag{4}$$

we were able to make an approximation of the dielectric constant. Where C is the parallel plate capacitor's capacitance, D is the sample's thickness, A its area, and ε_0 the permittivity of free space. In all the samples with an increase

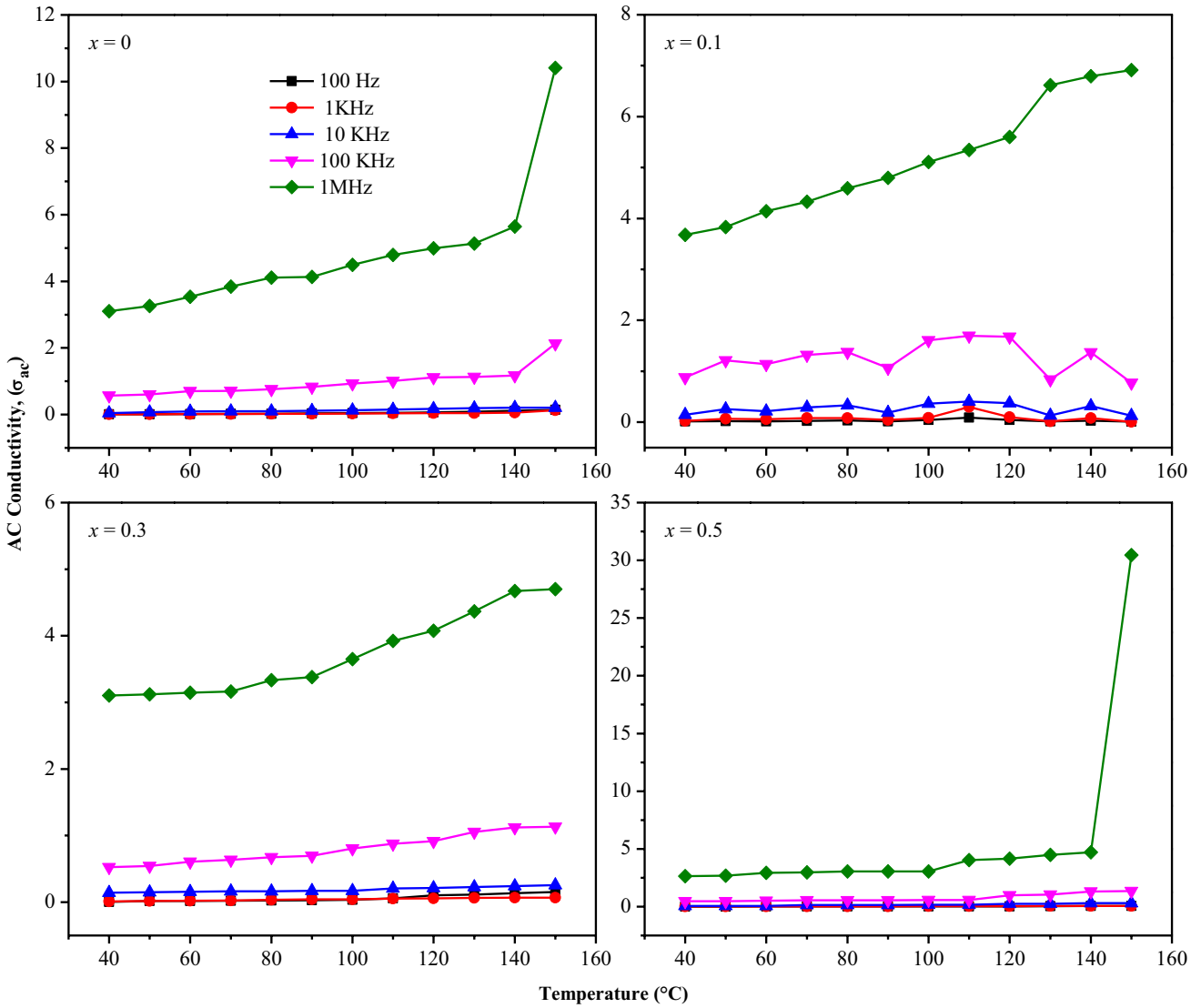

Fig. 11 A.C. Conductivity plots of Ni-doped $MgFe_2O_4$ spinel nanoparticles

in frequency, a drop in dielectric constant is seen owing to the varied polarisation mechanism of different frequencies. Polarization is a function of the ions' electronic orientation space-based electrical charge distribution [44, 45]. Surface flaws and oxygen vacancies may cause space charge polarisation to travel and capture (or be trapped) by the defects when an electric field is applied to the material [46]. Furthermore, owing to the electron exchange between Mg^{2+}/Ni^{2+} (A-site) to Fe^{3+} (B-site) the host materials were causing a larger dielectric constant at low frequency. However, at higher frequencies, the dielectric constant is lowered as the space charge is unable to maintain and fulfill the external field. Therefore, when frequency increases, polarisation weakens, resulting in a lower dielectric constant [46]. With an increase in temperature, ion diffusion in space charge polarisation is facilitated. Oxygen ion vacancies, on the other hand, might be interpreted as positive charges, leading to dipole moments in the direction of the applied field at the interface between nanomaterials. In turn, this causes a change in the polarization's direction [44]. According to Fig. 10, the dielectric constant increases with temperature, possibly because the molecules have enough thermal energy to orient themselves in the applied field at higher temperatures. Because the molecules in this material remain immobile in the solid state, the dielectric constant drops with decreasing temperature [47].

3.9 AC Conductivity

The investigation of ac conductivity yields data on the movement of charge carriers. The ac conductivity of Ni-doped

Table 3 The comparative studies of Ni doped $MgFe_2O_4$ spinel nanoparticles

Methods	Average crystallite size (nm)	Lattice parameter (Å)	Band gap (eV)	Magnetic properties	Dielectric properties (ε')	AC conductivity	References
Urea-assisted microwave combustion	Decreases: 20.65–17.05	Increases: 8.386–8.418	Increases: 1.81–2.31	Increases, Ms (emu/g): 32.79–57.95	–	–	[28]
Sol–gel method	Decreases: 34.96–30.94	Increases: 8.35–8.38	–	Increases, Ms (emu/g): 19.824–31.958	Decreases: 8.82–1.0 at 3 MHz	–	[46]
Solid state reaction	Increases: 930.0–1040.0	Increases: 8.332–8.375	–	–	The decrease of dielectric constant with increase in frequency	AC conductivity increases with increase in frequency	[47]
Classic ceramic method	Decrease: 38.3–26.8	–	Increase: 2.14–2.19	Ms (kOe): 3.76–16.1	–	–	[48]
Solvothermal reflux method	Increases: 8–12	Decreases: 8.376–8.363	–	Increases, Ms (emu/g): 40.72–48.78	–	–	[49]
Hydrothermal route	Increases: 25,000–33,000	–	Decreases: 2.58–2.29	Increases, Ms (emu/g): 9.949–21.80	The dielectric constant decreasing trend in terms of frequency	AC conductivity was increased with frequency	[50]
L-arginine assisted microwave combustion	Decreases: 26.0–17.0	Increases: 8.319–8.400	Decreases: 2.09–1.82	Increases, Ms (emu/g): 0.141–0.178	The dielectric constant increases with temperature	AC conductivity was increased with temperature	Present work

$MgFe_2O_4$ ($x = 0$, 0.1, 0.3, and 0.5) spinel nanoparticles were determined. The material's electrical conductivity σ_{ac} was determined via the following relation.

$$\sigma_{ac} = \omega \varepsilon_r A \tan \delta \varepsilon_0 \quad (5)$$

In this equation, ε_r stands for relative permittivity, $\tan \delta$ stands for loss tangent, and ε_0 stands for the vacuum dielectric constant (8.85×10^{12} Farad/m). The σ_{ac} vs T plots of Ni-doped $MgFe_2O_4$ ($x = 0$, 0.1, 0.3, and 0.5) spinel nanoparticles are depicted in Fig. 11, where the temperature is varied from 313 to 423 K, and frequency is varied from 100 Hz to 1 MHz, respectively. In all the samples it is noticed that conductivity is high at higher frequencies for all the samples which can be said as normal dielectric characteristics. The conductivity was found to be low at lower temperatures due to the lower number of vacancy sites. But with the increase in temperature, a greater number of defect sites are formed, which enhances the conductivity [47]. It is seen that Ni-doped $MgFe_2O_4$ ($x = 0.5$) sample exhibited the highest conductivity owing to the presence of a greater number of defect sites.

The comparative studies of $Mg_{1-x}Ni_xFe_2O_4$ ($x = 0$, 0.1, 0.3 and 0.5) spinel nanoparticles was discussed in Table 3.

4 Conclusions

Ni-doped $MgFe_2O_4$ NPs were prepared by MCM. The structure of magnesium ferrite inverse spinel is obtained from XRD patterns. XPS validated surface composition and valence states of Ni^{2+} doped $MgFe_2O_4$ spinel NPs. The average size of a crystallite is between 26 and 17 nm. The morphology of spinel nanoparticles was studied using HR-SEM images. The energy dispersive X-ray method is used for ensuring the presence of elements in the Ni^{2+} doped $MgFe_2O_4$ Nanoparticles. The band gap value in the range between 2.09, 2.02, 1.85, and 1.82 eV have been obtained using the Kubelka–Munk equation. The magnesium spinel structure is validated by the occurrence of the band at 434 and 561 cm^{-1} which corresponds to the stretching vibration of the octahedral site (Mg^{2+} -O^{2-}) and tetrahedral site (Fe^{3+} -O^{2-}) respectively. From the hysteresis curves the magnetic features viz. H_c, M_r, and M_s were determined. Further, the dielectric study is performed, owing to the presence of a greater number of defect sites, the Ni-doped $MgFe_2O_4$ ($x = 0.5$) sample exhibited the highest conductivity.

Acknowledgements The authors extend their sincere appreciation to the Researchers Supporting Project number (RSPD2023R682), King Saud University, Riyadh, Saudi Arabia for the support.

Author contributions Synthesis: RR, MS.Morphological and elemental analysis: MU, MG, SSS, BP,AK, NS. Magnetic studies: MS, CSD, AS. Dielectric studies: AU, CSD. Paper writing, result interpretation and idea conceived: MS, CSD, MS.

Funding This study was supported by Researchers Supporting Project number (RSPD2023R682), King Saud University, Riyadh, Saudi Arabia.

Declarations

Competing interests The authors declare no competing interests.

References

1. M. Sundararajan, L. John Kennedy, J. Environ. Chem. Eng. **5**, 4092 (2017)
2. A.T. Dhiwahar, S. Maruthamuthu, K.V. Chandekar, M.S. Hamdy, M. Shkir, M. Sundararajan, P. Sakthivel, Adv. Powder Technol. **32–11**, 4041 (2021)
3. M. Sundararajan, M. Sukumar, C.S. Dash, A. Sutha, S. Suresh, M. Ubaidullah, A.M. Al-Enizi, M.K. Raza, D. Kumar, Physica B **644**, 414232 (2022)
4. M. Agila, S. Krithiga, Int. J. Res. Eng. Sci. Manag. **2**(2), 475–482 (2019)
5. C.S. Dash, S.R. Prabaharan, Rev. Adv. Mater. Sci. **58**(1), 248–70 (2019)
6. M. Sukumar, J.R. Rajabathar, A.L. Hamad, S. Suresh, C.S. Dash, M. Sundararajan, P.S. Subudhi, S. Arokiyaraj, E. Yanmaz, S. Yuvaraj, R.R. Isaac, J. Alloys Compds. **953**, 169902 (2023)
7. S. Reddy, B.K. Swamy, U. Chandra, K.R. Mahathesha, T.V. Sathisha, H. Jayadevappa, Anal. Methods **3**(12), 2792–6 (2011)
8. V.A. Bharati, S.B. Somvanshi, A.V. Humbe, V.D. Murumkar, V.V. Sondur, K.M. Jadhav, J. Alloys Compds. **821**, 153501 (2020)
9. N. Subhashini, S. Revathi, M. Ubaidullah, A.M. Al-Enizi, S. Muthulakshmi, D. Thiripurasundari, S.F. Shaikh, A. Nafady, M.M. Abdulhameed, N.B. Alanzi, R.I. Alkhalifah, Dalton Trans. **52**(9), 2735–2748 (2023)
10. A. Maleki, P. Ravaghi, M. Aghaei, H. Movahed, Res. Chem. Intermed. **43**, 5485–5494 (2017)
11. M. Sukumar, M. Agila, A. Sutha, V. Ravi, A.M. Al-Enizi, M. Ubaidullah, M.S. Samdani, M. Sundararajan, B. Pandit, J. Mater. Sci. Mater. Electron. **33**(35), 26144–56 (2022)
12. L. Zheng, K. Fang, M. Zhang, Z. Nan, L. Zhao, D. Zhou, M. Zhu, W. Li, RSC Adv. **8**, 39177–39181 (2018)
13. D. Chen, D. Li, Y.Z. Zhang, Z. Kang, Ultrason. Sonochem. **20**(6), 1337–1340 (2013)
14. S. Samiei, F. Pakpour, D. Ghanbari, J. Nanostruct. **8**(1), 37–46 (2018)
15. A. Maleki, M. Kamalzare, Tetrahedron Lett. **55**, 6931–6934 (2014)
16. A. Maleki, J. Rahimi, J. Porous Mater. **25**, 1789–1796 (2018)
17. M.R. Ahghari, V. Soltaninejad, A. Maleki, Sci. Rep. **10**, 12627 (2020)
18. N. Kumar, R. Singh, H. Satyapal, J. Mater. Sci. Mater. Electron. **31**, 9231–9241 (2020)
19. E. Suharyadi, A. Hermawan, D.L. Puspitarum, J. Phys. Conf. Ser. **1091**, 012003 (2018)
20. S. Kanithan, N.A. Vignesh, K.M. Katubi, P.S. Subudhi, E. Yanmaz, J.A. Dhanraj, N.S. Alsaiari, M. Sukumar, M. Sundararajan, S. Baskar, S. Sahu, J. Mol. Struct. **1265**, 133289 (2022)
21. Z. Thompson, S. Rahman, S. Yarmolenko, J. Sankar, D. Kumar, N. Bhattarai, Materials **10**(1–12), 937 (2017)
22. S.I. Hussein, A.S. Elkady, M.M. Rashad, A.G. Mostafa, R.M. Megahid, J. Magn. Magn. Mater. **379**, 9–15 (2015)
23. K. Mathankumar, M. Sukumar, C.S. Dash, M. Sundararajan, M. Ubaidullah, A.M. Al-Enizi, A. Sutha, M. Kausar Raza, J. Arockia Dhanraj, D. Kumar, J. Inorg. Organomet. Polym. **32**, 3476–3487 (2022)
24. L.T.H. Nguyen, N.C. Manh, D.N. Quoc, H.N. Quang, H.T.T. Nguyen, D.C. Nguyen, L.G. Bach, J. Chemother. (2019). https://doi.org/10.1155/2019/3428681
25. M. Sukumar, L. John Kennedy, J. Judith Vijaya, B. Al-Najar, M. Bououdina, New J. Chem. **42**, 18142 (2018)
26. M. Sundararajan, J. Vidhya, R. Revathi, M. Sukumar, V. Ravi, R. Rajkumar, M. Kamala Kannan, C.S. Dash, H. Lohedan, R. JothiRamalingam, S. Arokiyaraj, J. Ovonic Res. **17**, 479–486 (2021)
27. P.A. Udhaya, T.C. Bessy, M. Meena, Mater. Today: Proc. **8**, 169–175 (2019)
28. E. Hema, A. Manikandan, P. Karthika, M. Durka, S. ArulAntony, B.R. Venkatraman, J. Nanosci. Nanotechnol. **16**, 7325–7336 (2016)
29. A. Parveez, S.A. Khader, J. Chem. Pharm. Sci. **9**, 998–1002 (2016)
30. L. Phor, S. Chahal, V. Kumar, J. Adv. Ceram. **9**(5), 576–587 (2020)
31. A. Maleki, H. Movahed, P. Ravaghi, T. Kari, RSC Adv. **6**, 98777–98787 (2016)
32. F.H. Afruzi, F. Esmailzadeh, S. Asgharnasl, F. Ganjali, R.T. Ledari, A. Maleki, Sep. Purif. Technol. **291**, 120956 (2022)
33. M. Sukumar, L. John Kennedy, J. Judith Vijaya, B. Al-Najar, M. Bououdina, G. Mudhana, Vacuum **167**, 415 (2019)
34. A. Abu El-Fadl, A.M. Hassan, M.A. Kassem, Phys. Scr. **95**, 055813 (2020)
35. A. Maleki, M. Mohammad, Z. Emdadi, N. Asim, M. Azizi, J. Safaei, Arab. J. Chem. **13**, 3017–3025 (2020)
36. A. Maleki, Z. Hajizadeh, V. Sharifi, Z. Emdadi, J. Clean. Prod. **215**, 1233–1245 (2019)
37. J.R. Sen, P. Jain, R. Patidar, S. Srivastava, R.S. Rana, N. Gupta, Mater. Today **2**, 3750–3757 (2015)
38. D. Narsimulu, B. Nageswara Rao, M. Venkateswarlu, E.S. Srinadhu, N. Satyanarayana, Ceram. Int. **42**(15), 16789 (2016)
39. A. Maleki, Z. Hajizadeh, R.F. Haji, Microporous Mesoporous Mater. **259**, 46–53 (2018)
40. A. Maleki, T. Kari, M. Aghaei, J. Porous Mater. **24**, 1481–1496 (2017)
41. S.U. Bhasker, Y. Veeraswamy, N. Jayababu, M.V. Ramanareddy, Mater. Today Proc. **3**, 3666 (2016)
42. N. Senthil Kumar, M. Ganapathy, S. Sharmila, M. Shankar, M. Vimalan, I. Vetha Potheher, J. Alloys Compds. **703**, 624–632 (2017)
43. Dennis Raj, M. Jeeva, R. Purusothaman, G. Venkatesa Prabhu, M. Vimalan, I. Vetha Potheher, J. Mater. Sci: Mater Electron. 10.1007/s10854-017-6476.
44. N. Senthilkumar, M. Ganapathy, A. Arulraj, M. Meena, M. Vimalan, I.V. Potheher, J. Alloys Compds. **750**, 171–181 (2018)
45. A. Vinosha, E. Jeronsia, K. Raja, A. christina Fernandez, S. Krishnan, J. Das, Optik **127**(20), 9917–9925 (2016)
46. G. Asghar, E. Tariq, S.N. Khisro, G.H. Tariq, M.S. Awan, M.A. Khan, Y. Iqbal, K. Safeen, M. Anis-ur-Rehman, Kuwait J. Sci. (2023). https://doi.org/10.1016/j.kjs.2023.05.001
47. P. Chavan, L.R. Naik, Vacuum **152**, 47–49 (2018)
48. S. Sarıtas, B.C. Sakar, M. Kundakci, B. Gürbulak, M. Yıldırım, Mater. Today **46**, 6920–6923 (2021)
49. A. Manohar, V. Vijayakanth, M.R. Pallavolu, K.H. Kim, J. Alloys Compds. **879**, 160515 (2021)

50. N. Khaliq, I. Bibi, F. Majid, M.I. Arshad, A. Ghafoor, Z. Nazeer, S. Ezzine, N. Alwadai, A. Nazir, M. Iqbal, Results Phys. **43**, 106059 (2022)